ChemComm

COMMUNICATION

View Article Online
View Journal | View Issue

Cite this: *Chem. Commun.*, 2026, **62**, 3334

Received 29th September 2025,
Accepted 6th January 2026

DOI: 10.1039/d5cc05562h

rsc.li/chemcomm

Solvent-dependent self-assemblies with multi-inverted circularly polarized luminescence based on 9,10-distyrylanthracene

Meng Wang, Yuxuan Song, Zhixuan Wang, Bin Xu * and Wenjing Tian *

Ordered self-assembly of the amphiphilic aggregation-induced emission molecule DSA-Chol yielded assemblies with outstanding chiral luminescent properties. Modulation of the poor solvent ratio led to significant amplification and multiple inversions of the CPL signals of the assemblies.

Circularly polarized luminescence (CPL) from organic small molecules can be significantly enhanced through self-assembly into ordered aggregates, often resulting in an order-of-magnitude increase in the luminescence dissymmetry factor (g_{lum}). Generally, it's because of the "sergeants-and-soldiers" principle and the "majority-rules" effects in the aggregated state.[1] However, conventional luminescent molecules such as anthracene, pyrene, and perylene suffer from aggregation-caused quenching (ACQ), which decreases the fluorescence quantum yield (QY, Φ) of their aggregate states. The emergence of aggregation-induced emission (AIE) luminogens, first reported by Tang *et al.*, has provided an effective strategy to overcome ACQ, thereby enabling the simultaneous realization of high g_{lum} and QY.[2]

Among AIE-active systems, 9,10-distyrylanthracene (DSA) represents a typical structural motif with a twisted geometry. CPL materials based on DSA generally exist as small molecules[3] or co-assemblies.[4] However, the DSA framework combines π–π interactions from the anthracene unit with orientation control from terminal substituents, making it an attractive platform for constructing supramolecular assemblies. Achieving ordered assembly of DSA derivatives is therefore expected to be highly beneficial for tuning both the aggregation structure and chiral photophysical properties. Nevertheless, key challenges remain in molecular design strategies that enable ordered assembly and in regulating supramolecular performance through controllable intermolecular interactions. Previous studies have shown that modification of terminal groups can drive the assembly of DSA derivatives and modulate their optical properties, although excited-state chirality was not realized.[5] Our group has also investigated optically active DSA-based materials in various aggregated states, including crystals,[6] nanoparticles,[7] and gels.[8] Based on previous research, the cholesteryl (Chol) group was introduced at both ends of the DSA core. It not only served as a chiral source but also provided strong hydrophilicity, which helps alleviate the torsional structure of DSA and promotes the formation of ordered self-assembled micro-/nanostructures. The resulting amphiphilic molecule, termed DSA-Chol, was subsequently investigated for its self-assembly behavior in systems using water or methanol as the poor solvent. Not only were assemblies with excellent g_{lum} and QY achieved, but also amplified or opposite CPL signals could be obtained merely by adjusting the solvent proportion. The study provides a new insight into the relationship among supramolecular environment, aggregation structure, and excited-state chirality.

The molecular structure of DSA-Chol is presented in Fig. 1a, which was confirmed by nuclear magnetic resonance (NMR) and mass spectrometry (MS) (Fig. S1–S3). The frontier molecular orbitals and UV-vis absorption spectra in the ground state were calculated by density functional theory (DFT) and analysed by Multiwfn,[9] which were consistent with the experimental results (Fig. S4 and S5). In dilute THF solution (8.07×10^{-5} M), DSA-Chol displayed absorption bands at 302 nm, attributed to the styryl group, and at 411 nm, assigned to a π–π* transition. Compared with the previously reported spectra of the DSA core, the attachment of Chol groups induced slight blue shifts in both the absorption and emission peaks.[10] In addition, the solid powder of DSA-Chol exhibited an emission maximum at 500 nm with a QY of 55.75%. The blue shift of the emission compared to that in dilute solution was mainly attributed to the reduced degree of molecular conjugation and the suppression of non-radiative transitions in the solid state. Upon assembly in THF/H_2O mixtures, the absorption spectra exhibited slight shifts with increasing water fraction (f_w) (Fig. 1b). These small variations, only a few nanometers, cannot

State Key Laboratory of Supramolecular Structure and Materials, College of Chemistry, Jilin University, Changchun 130012, P. R. China.
E-mail: xubin@jlu.edu.cn, wjtian@jlu.edu.cn

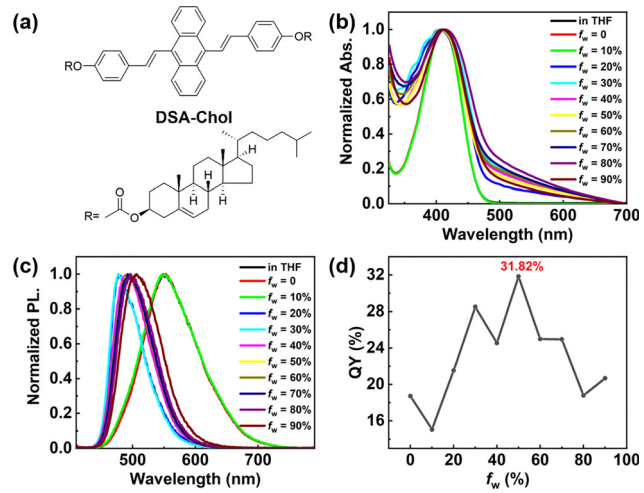

Fig. 1 (a) Chemical structure of DSA-Chol. (b) Absorption spectra, (c) emission spectra and (d) fluorescence quantum yields of the self-assembly systems under different water fractions. [DSA-Chol] = 8.07×10^{-5} M in a THF/H_2O mixture (v/v). The excitation wavelength (λ_{ex}) of the emission spectra was 400 nm.

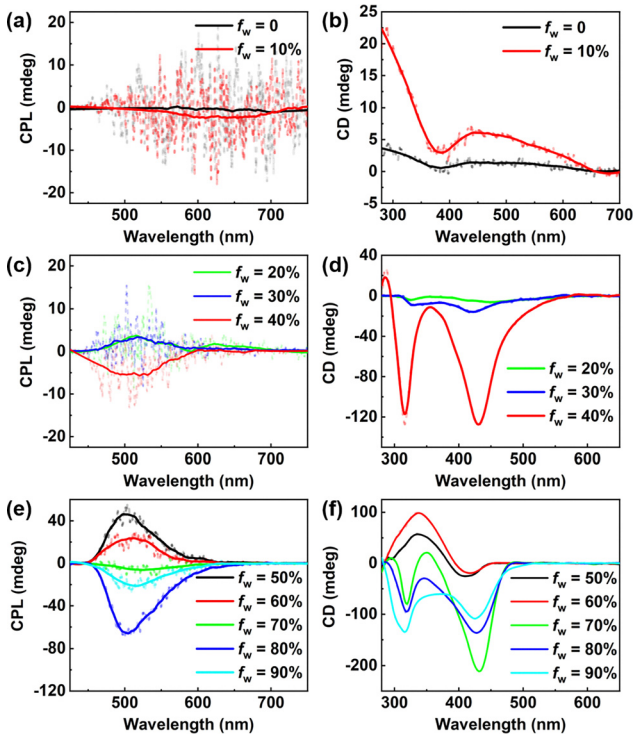

Fig. 2 Chiroptical properties of DSA-Chol self-assemblies. (a) CPL spectra and (b) CD spectra under ultra-low water content (f_w = 0–10%). (c) CPL spectra and (d) CD spectra under low water content (f_w = 20–40%). (e) CPL spectra and (f) CD spectra under high water content (f_w = 50–90%). [DSA-Chol] = 8.07×10^{-5} M in THF/H_2O mixture (v/v). λ_{ex} of the CPL spectra was 400 nm.

be simply attributed to J- or H-type aggregation, likely due to the intrinsic torsional flexibility of the DSA core. The emission spectra of DSA-Chol in THF solution also showed blue shifts that diminished with increasing f_w, indicating changes in the relative populations of aggregate species (Fig. 1c). In parallel, the QY increased progressively with the increase of water content, consistent with AIE characteristics (Fig. 1d), and the maximum QY of 31.82% was achieved at f_w of 50% (Table S1). Further addition of water led to reduced luminescence QY, which may result from the decreased structural order arising from altered intermolecular interactions at high f_w.[11]

The chiral optical properties of the assemblies at different f_w were investigated (Fig. 2). Based on their spectral features, the f_w values were divided into three regimes: ultra-low (0–10%), low (20–40%), and high (50–90%). To eliminate interference from linear polarization and birefringence, all measurements were repeated with sample rotation in the optical path.[12] At f_w of 10%, the emission spectrum of DSA-Chol showed little change compared with that in dilute solution; however, a detectable negative CPL signal emerged in the 500–700 nm range, consistent with the emission profile (Fig. 2a). The corresponding CD signal in the ground state was also more pronounced than that at f_w of 0, indicating that even ultra-low water content can induce partial aggregation and enhance chirality. At higher f_w values, CPL signals appeared in the 450–600 nm region, again matching the emission spectra. Positive CPL signals were observed at f_w of 20% and 30%, whereas a negative signal appeared at f_w of 40% (Fig. 2c). Further increasing f_w to 50% reversed the CPL from negative to positive, accompanied by an amplification of g_{lum} to $+7.28 \times 10^{-3}$ (about 2–3 times that of the low-f_w systems, Fig. S7 and Table S2). To confirm the anomalous negative signal at f_w of 40%, additional measurements at f_w of 35% and 45% were performed. The results showed a reasonable trend of chiral variation between 30% and 50% water content (Fig. S8 and S9). In the high-f_w regime, CPL inversion was also observed: a positive signal at f_w of 50–60% but a negative one at f_w of 70–90% (Fig. 2e). The maximum g_{lum} value of -1.08×10^{-2} was recorded at f_w of 80%. Furthermore, the ground-state CD spectra at f_w of 40% and 70–90% exhibited similar features, supporting the reliability of the CPL inversion observed under these conditions (Fig. 2d and f). In other words, DSA-Chol exhibited solvent-dependent CPL behavior with multiple signal inversions across different water fractions (Fig. S7).

To investigate the origin of the multiple CPL inversions, the morphological evolution of the assemblies was examined. At f_w of 10%, DSA-Chol formed ordered aggregates consisting of entangled *M*-helical nanofibers (Fig. S10). With increasing water content, numerous nanoribbons emerged, and at f_w of 30%, thinner nanosheet structures appeared (Fig. 3a). The proportion of nanosheets reached a maximum at f_w of 40% (Fig. 3b). The nanoribbons had a relatively small width and a thickness of approximately several tens of nanometers (Fig. 3c). In contrast, the nanosheets were much wider but less than 1 nm in thickness (Fig. 3d). These structural differences likely arise from subtle changes in molecular orientation within and perpendicular to the two-dimensional plane as influenced by water content (Fig. S12). At f_w of 50%, the formation of the nanosheet became unfavorable, resulting in a sharp decrease of nanosheet proportion (Fig. S13a). Correlating the

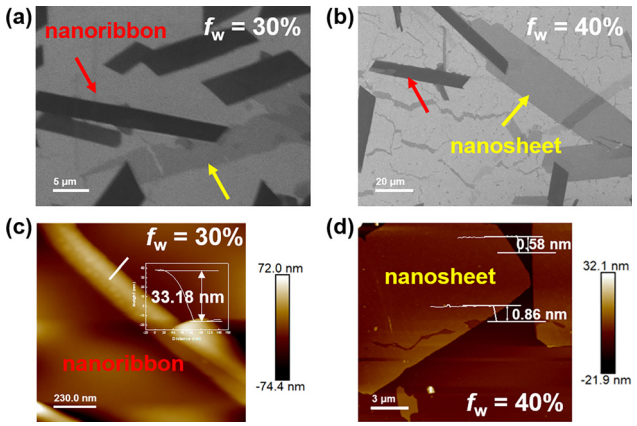

Fig. 3 Solvent-dependent morphological changes of the DSA-Chol self-assemblies. SEM images obtained at (a) 30% and (b) 40% water fraction. AFM images of (c) the nanoribbons obtained at water 30% fraction and (d) the nanosheets obtained at 40% water fraction.

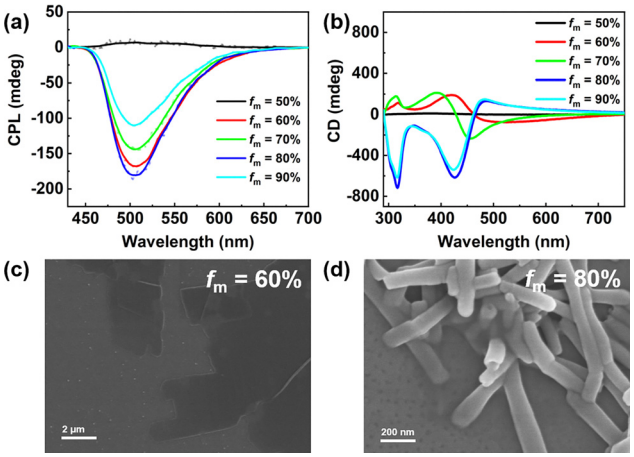

Fig. 4 Chiroptical properties and morphological changes of DSA-Chol assemblies in anhydrous systems. (a) CPL spectra (λ_{ex} = 400 nm) and (b) CD spectra under different methanol fractions (f_m = 50–90%). SEM images obtained at (c) 60% and (d) 80% methanol fraction. [DSA-Chol] = 8.07 × 10^{-5} M in THF/methanol mixture (v/v).

morphological and CPL data, we speculated that nanoribbons are the source of positive CPL signal. At f_w of 40%, the increased presence of nanosheets suppressed the nanoribbon contribution, leading to a negative signal, whereas at f_w of 50%, the reduced nanosheet fraction restored the dominance of the nanoribbons and the positive CPL response. This may also be the reason for the abnormal decrease of QY at f_w of 40% in Fig. 1d, *i.e.*, the AIE effect of nanosheet structures is inferior to that of nanoribbons. Afterwards, at f_w of 60%, the formation of nanoribbons became difficult (Fig. S13b), accompanied by a weakening of the positive signal. But from the transmission electron microscopy (TEM) images, we could observe some *P*-chiral nanofibers, which were opposite to the helical direction of the fibers at f_w of 10%. The CPL signals of these two states were likewise opposite, confirming chirality transfer and inversion at the supramolecular level. When f_w reached 70%, most assemblies fragmented into small domains, and further increases in water content produced increasingly disordered morphologies (Fig. S13c–e). This transition coincided with the disappearance of nanoribbons and the emergence of negative CPL signals.

To assess whether the tunable CPL behavior is universal in DSA-Chol assemblies and to clarify the role of water, methanol was used as an alternative poor solvent. The effect of varying methanol fractions (f_m) on assembly morphology and optical properties was systematically examined. At low f_m values (10–40%), the assemblies showed negligible CPL signals, and analysis therefore focused on high-f_m conditions. At f_m of 50%, the CD signal in the ground-state was weak, but in the excited state, it exhibited a distinct positive CPL response with a maximum g_{lum} of +2.12 × 10^{-3} at 476 nm (Fig. 4a, b and Fig. S20). At this stage, DSA-Chol assembled into strip-like macroscopic structures, morphologically similar to those at f_m of 40%. Notably, some strips twisted into *P*-helical microribbons (Fig. S15b), which likely accounted for the emergence of the positive CPL signal. No smaller ordered structures were detected by TEM. A further increase of f_m (60–70%) produced nanosheets (Fig. 4c and Fig. S16a, S17a) accompanied by intense negative CPL signals (Fig. 4a). These nanosheets differed markedly from those formed in aqueous systems, and were about 4 nm thick and stacked in a layer-by-layer fashion (Fig. S18). At f_m of 60%, the QY reached 38.18%, surpassing the maximum value observed in water (Fig. S19). When f_m was increased to 80–90%, the assemblies maintained strong negative CPL signals, but their morphology transitioned into hollow nanotubes (Fig. 4d and Fig. S16b, S17b). The nanotube walls were substantially thicker than the nanosheets at f_m of 60%. Powder X-ray diffraction (PXRD) analysis suggested that this transformation originated from altered intermolecular interactions rather than spontaneous curling of nanosheets (Fig. S21d). Importantly, the strongest CPL response was achieved at f_m of 80%, with a g_{lum} of −2.18 × 10^{-2}, again exceeding the maximum value obtained in aqueous systems (Fig. S20). Therefore, replacing water with methanol as the poor solvent not only preserved the CPL inversion behavior but also enabled overall superior optical performance, with higher QY and g_{lum} values.

To gain insight into the assembly mechanism, PXRD and Fourier-transform infrared (FT-IR) analyses were performed. At f_w of 10–40%, the assemblies exhibited multiple PXRD reflections, indicating relatively high crystallinity. From the Bragg equation, the 2θ value of 18.26° corresponded to a *d*-spacing of 0.49 nm (Fig. S21a). At higher water fractions (f_w of 50–90%), the diffraction peaks shifted markedly and the overall crystallinity decreased. A 2θ value of 29.38° gave a reduced *d*-spacing of 0.30 nm, which can be attributed to the enhanced π–π interactions (Fig. S21b).[13] Although nanoribbons remained the dominant morphology at f_w of 50–60%, their molecular packing became denser, and the enhanced exciton coupling between chromophores led to pronounced amplification of the CPL signals compared with the low-f_w regime.[14] The FT-IR spectra further confirmed the role of water in the assembly process. A distinct absorption band near 3450 cm^{-1} appeared,

which was assigned to O–H stretching of water molecules, as DSA-Chol itself contains no O–H or N–H groups (Fig. S21c).[15] The normalized intensity of this band reflected the degree of water participation in the assemblies. In contrast, the methanol-based assemblies did not show analogous O–H bands in their FT-IR spectra (Fig. S22), but their PXRD patterns reflected morphological changes. At f_m of 40–50%, strip-like structures yielded a consistent diffraction peak at 2θ of 14° (Fig. S23b). At f_m of 60–70%, a peak at 29.34° corresponded to a *d*-spacing of 0.30 nm, confirming that denser π–π stacking drove nanosheet formation and CPL amplification (Fig. S21d). At f_m of 80–90%, the PXRD peak shifted to 2θ of 5.96°, giving a *d*-spacing of 1.48 nm, indicative of assemblies lacking π–π interactions (Fig. S23a). Despite the consistently negative CPL signals observed at f_m of 60–90%, the results revealed distinct differences in molecular packing modes across these conditions.

Single crystals of DSA-Chol were successfully obtained (CCDC: 2518722). As shown in Fig. S24, the crystal structure revealed a packing mode consistent with that of the dominant nanoribbon assemblies formed under low water content.[16] The diffraction peak at 2θ of 18.26° corresponded to the (022) crystal plane, with a calculated *d*-spacing in agreement with the PXRD results. The anthracene moieties of adjacent molecules exhibit distinct offset stacking (though they are separated by 0.38 nm), thus there may be no π–π interactions from the anthracene rings (Fig. S25). X-ray crystallographic analysis further revealed a triclinic lattice with space group *P*1, characteristic of a *J*-aggregated crystal (Fig. S27). The intermolecular interactions were dominated by short contacts, including C–H···H–C (2.395, 2.361, and 2.202 Å) and C–H···O (2.660 Å) interactions (Fig. S28). This packing mode, which does not rely on π–π stacking of anthracene moieties, is key to stabilizing the nanoribbons observed under low water content in aqueous systems.

In summary, we designed an amphiphilic molecule, DSA-Chol, by incorporating an AIE-active DSA unit. The molecule undergoes ordered self-assembly in aqueous systems, where water serves as the poor solvent, leading to excellent CPL performance accompanied by multiple inversions of excited-state chiral signals. When methanol was used as the poor solvent, the CPL activity was further enhanced. The tunable CPL behavior can be attributed to variations in both intermolecular and solvent–molecule interactions under different solvent conditions. These findings provide new insights into the precise regulation of supramolecular structures and the optimization of material performance in the framework of supramolecular chemistry.

This work was supported by the National Natural Science Foundation of China (No. 22275065, 52073116 and 52473177) and the Natural Science Foundation of Jilin Province (No. 20240101003JJ).

Conflicts of interest

There are no conflicts to declare for the authors.

Data availability

All data generated or analysed during this study are included in the manuscript, supplementary information (SI) and crystallographic data. Supplementary information is available. See DOI: https://doi.org/10.1039/d5cc05562h.

CCDC 2518722 contains the supplementary crystallographic data for this paper.[17]

References

1 W. Chen, B. Li, G. Gao and T. Sun, *Interdiscip. Mater.*, 2023, **2**, 689–713.
2 (*a*) J. Mei, N. L. C. Leung, R. T. K. Kwok, J. W. Y. Lam and B. Z. Tang, *Chem. Rev.*, 2015, **115**, 11718–11940; (*b*) H. Yan, Y. He, D. Wang, T. Han and B. Z. Tang, *Aggregate*, 2023, **4**, e331; (*c*) M. Wang, Z. Wang, L. Liu and W. Tian, *J. Mater. Chem. C*, 2025, **13**, 20880–20920.
3 W.-J. Li, Q. Gu, X.-Q. Wang, D.-Y. Zhang, Y.-T. Wang, X. He, W. Wang and H.-B. Yang, *Angew. Chem., Int. Ed.*, 2021, **60**, 9507–9515.
4 (*a*) X.-Y. Lou, K. Zhang, Y. Bai, S. Zhang, Y. Li and Y.-W. Yang, *Angew. Chem., Int. Ed.*, 2025, **64**, e202414611; (*b*) Y. Guo, Y. Han, X.-S. Du and C.-F. Chen, *ACS Appl. Polym. Mater.*, 2022, **4**, 3473–3481; (*c*) Y.-Q. Zhu, Z. Chen, Z.-Y. Chen, Z.-W. Zhou, Q. Bai, M.-X. Wu and X.-H. Wang, *Chem. – Eur. J.*, 2024, **30**, e202402808.
5 (*a*) X. Gou, J. Lu, H.-Y. Zhao, Y.-R. Pei and L. Y. Jin, *Soft Matter*, 2023, **19**, 6683–6690; (*b*) X. Gou, N. Ye, Q. Han, J. Cui and L. Yi Jin, *J. Mol. Liq.*, 2024, **393**, 123636.
6 (*a*) Y. Liu, A. Li, S. Xu, W. Xu, Y. Liu, W. Tian and B. Xu, *Angew. Chem., Int. Ed.*, 2020, **59**, 15098–15103; (*b*) B. Shao, R. Jin, A. Li, Y. Liu, B. Li, S. Xu, W. Xu, B. Xu and W. Tian, *J. Mater. Chem. C*, 2019, **7**, 3263–3268; (*c*) S. Ma, J. Zhang, Y. Liu, J. Qian, B. Xu and W. Tian, *J. Phys. Chem. Lett.*, 2017, **8**, 3068–3072.
7 W. Han, Y. Du, M. Song, K. Sun, B. Xu, F. Yan and W. Tian, *J. Mater. Chem. B*, 2020, **8**, 9544–9554.
8 J. Feng, Z. Gu, W. Ma, S. Jiang, Y. Jiao, L. Liu, B. Xu and W. Tian, *J. Phys. Chem. C*, 2021, **125**, 21270–21276.
9 (*a*) T. Lu and F. Chen, *J. Comput. Chem.*, 2012, **33**, 580–592; (*b*) T. Lu, *J. Chem. Phys.*, 2024, **161**, 082503.
10 J. He, B. Xu, F. Chen, H. Xia, K. Li, L. Ye and W. Tian, *J. Phys. Chem. C*, 2009, **113**, 9892–9899.
11 L. Yao, K. Fu and G. Liu, *ACS Appl. Mater. Interfaces*, 2023, **15**, 40817–40827.
12 (*a*) C. Zhao, Y. Wang, Y. Jiang, N. Wu, H. Wang, T. Li, G. Ouyang and M. Liu, *Adv. Mater.*, 2024, **36**, 2403329; (*b*) Z.-F. Liu, X.-X. Liu, H. Zhang, L. Zeng, L.-Y. Niu, P.-Z. Chen, W.-H. Fang, X. Peng, G. Cui and Q.-Z. Yang, *Angew. Chem., Int. Ed.*, 2024, **63**, e202407135.
13 Y.-J. Wang, X.-Y. Shi, Y. Guo, X.-N. Wang, K.-X. Zheng, X.-W. Yang, P. Xing and S.-Q. Zang, *J. Am. Chem. Soc.*, 2025, **147**, 5408–5416.
14 (*a*) S. E. Penty, G. R. F. Orton, D. J. Black, R. Pal, M. A. Zwijnenburg and T. A. Barendt, *J. Am. Chem. Soc.*, 2024, **146**, 5470–5479; (*b*) Y. Wang, N. Li, L. Chu, Z. Hao, J. Chen, J. Huang, J. Yan, H. Bian, P. Duan, J. Liu and Y. Fang, *Angew. Chem., Int. Ed.*, 2024, **63**, e202403898.
15 S. Dong, J. Leng, Y. Feng, M. Liu, C. J. Stackhouse, A. Schönhals, L. Chiappisi, L. Gao, W. Chen, J. Shang, L. Jin, Z. Qi and C. A. Schalley, *Sci. Adv.*, 2017, **3**, eaao0900.
16 S. Wu, X. Song, J. Lu, W. Hao and M. Liu, *Angew. Chem., Int. Ed.*, 2025, **64**, e202421108.
17 CCDC 2518722: Experimental Crystal Structure Determination, 2026, DOI: 10.5517/ccdc.csd.cc2qjy3b.